https://doi.org/10.5194/tc-2020-147
Preprint. Discussion started: 16 July 2020

The Cryosphere Discussions

Grounding zone subglacial properties from calibrated active source seismic methods

Huw J. Horgan[1], Laurine van Haastrecht[1], Richard B. Alley[2], Sridhar Anandakrishnan[2], Knut Christianson[3], and Atsuhiro Muto[4]

[1]Antarctic Research Centre, Victoria University of Wellington, Wellington, New Zealand
[2]Department of Geosciences and Earth and Environmental Systems Institute, Pennsylvania State University, University Park, Pennsylvania 16802, USA
[3]Earth and Space Sciences, University of Washington, Seattle, Washington 98195, US
[4]Department of Earth and Environmental Science, Temple University, Philadelphia, Pennsylvania 19122, USA

Correspondence: Huw Horgan (huw.horgan@vuw.ac.nz)

Abstract. The grounding zone of Whillans Ice Stream, West Antarctica, exhibits an abrupt transition in basal properties from the grounded ice to the ocean cavity over distances of less than 0.5–1 km. Active source seismic methods reveal the grounded portion of the ice stream is underlain by a relatively stiff substrate (relatively high shear wave velocities) compared to the deformable till found elsewhere beneath the ice stream. Several kilometers upstream of the grounding zone, layers of subglacial water are detected, as are regions that appear to be water layers less than the thickness resolvable by our technique. The presence of stiff subglacial sediment and thin water layers upstream of the grounding zone supports previous studies that have proposed the dewatering of sediment within the grounding zone and the possibility that ocean water is pumped into the subglacial system and upstream. The setting enables calibration of our methodology using returns from the floating ice shelf. This allows a comparison of different techniques used to estimate the sizes of the seismic sources. We find a strong correlation (coefficient of determination=0.45) between our calibrated method and a commonly used amplitude ratio method, but our results also highlight the incomplete knowledge of other factors affecting the amplitude of seismic sources and reflections in the cryosphere.

1 Introduction

Grounding zones mark the transition from grounded to floating ice, standing sentinel over much of the contribution of glaciers and ice sheets to sea level. Grounding zones are actively built and modified, with sedimentation at grounding zones providing temporary stabilisation of their position against small increases in sea level (Anandakrishnan et al., 2007; Alley et al., 2007) and tidal working of the sediments strengthening the bed of the ice (Walker et al., 2013). Ice flux across the grounding zone is highly sensitive to ice thickness, leading to the potential for runaway grounding zone retreat of marine ice sheets with inward

https://doi.org/10.5194/tc-2020-147
Preprint. Discussion started: 16 July 2020


The Cryosphere Discussions

sloping beds (Schoof, 2007). The grounding zone transition from limited basal slip beneath an ice stream to zero traction beneath an ice shelf has proved a challenge to simulate numerically (Barcilon and MacAyeal, 1993; Nowicki and Wingham, 2008) and abrupt transitions occurring over length scales comparable to an ice thickness may require the full Stokes equations to be solved if grounding zone dynamics are to be accurately simulated (Pattyn et al., 2013).

Here we investigate the grounding zone of Whillans Ice Stream, Siple Coast, West Antarctica (Figure 1). Upstream of the grounding zone, deformable sediments underlie the Siple Coast ice streams, enabling their fast flow in the absence of high driving stress (Kamb, 2001; Alley et al., 1986, 1987; Blankenship et al., 1987; Alley et al., 1989; Anandakrishnan et al., 1998). Regions of high basal drag known as sticky spots balance a significant proportion of driving stress (Alley, 1993; MacAyeal et al., 1995) and likely correspond with regions of the bed that have relatively less subglacial water than surrounding regions (Anandakrishnan and Alley, 1994; Winberry et al., 2011; Luthra et al., 2016, 2017). Ice stream beds tend to get smoother farther downglacier (Siegert et al., 2004) suggesting that subglacial sediment thickness is increasing as the grounding zone is approached, as sediment is transported downstream englacially and subglacially (Alley et al., 1989) before ultimately being deposited in the ocean cavity. Observations and modelling of flexure and internal-layer deformation within the ice column indicate that subglacial sediment may stiffen beneath the grounding zone (Walker et al., 2013; Christianson et al., 2013). Ice flexure at the grounding zone may also act to draw ocean water into the subglacial system at low tide and force it upstream at high tide (Walker et al., 2013; Horgan et al., 2013a). Dewatering and stiffening of suglacial material at the grounding zone is also consistent with a sticky-spot located near the grounding zone identified using geodetic observations of the diurnal stick–slip cycle of Whillans Ice Stream (Winberry et al., 2011; Pratt et al., 2014).

To investigate the basal properties beneath Whillans Ice Stream's grounding zone, and the distance over which the transition to the freely slipping ice shelf occurs, we use active source seismic techniques that are commonly applied in studies addressing the basal boundary of glaciers and ice sheets (e.g. Anandakrishnan, 2003; Smith, 2007; Brisbourne et al., 2017; Zechmann et al., 2018; Muto et al., 2019). These methods require the source amplitude and path effects to be estimated, which is often challenging due to variability in source and receiver coupling, and strong vertical gradients in density and seismic velocity in the firn. Acquiring data over the ocean cavity allows calibration of these methods due to the presence of a known reflection interface. This enables a robust estimate of subglacial properties at a spatial resolution of less than an ice thickness.

2 Data and Methods

Here we present amplitude analysis of data from four transects across the grounding zone of Whillans Ice Stream (Figure 1) acquired in the austral summer of 2011/2012. Acquisition was composed of an explosive seismic source detonated at approximately 27 m depth, with charge sizes of 0.4 kg (Line 1) and 0.8 kg (Lines 2, and 4) and 0.85 kg (Line 3) at a nominal shot spacing of 240 m. Each of Line 3's 0.85 kg charge was composed of one 0.4 kg charge and three narrower 0.15 kg charges. All other charges were composed of equal diameter 0.4 kg charges. The time between burial and detonation varied but always exceeded 24 hours. Geophones were buried approximately 0.5 m beneath the snow surface at 20 m spacings, and consisted of alternating single-string 40 Hz geophones (even channels) and 5-element 40 Hz georods (odd channels, Voigt et al., 2013).

https://doi.org/10.5194/tc-2020-147
Preprint. Discussion started: 16 July 2020

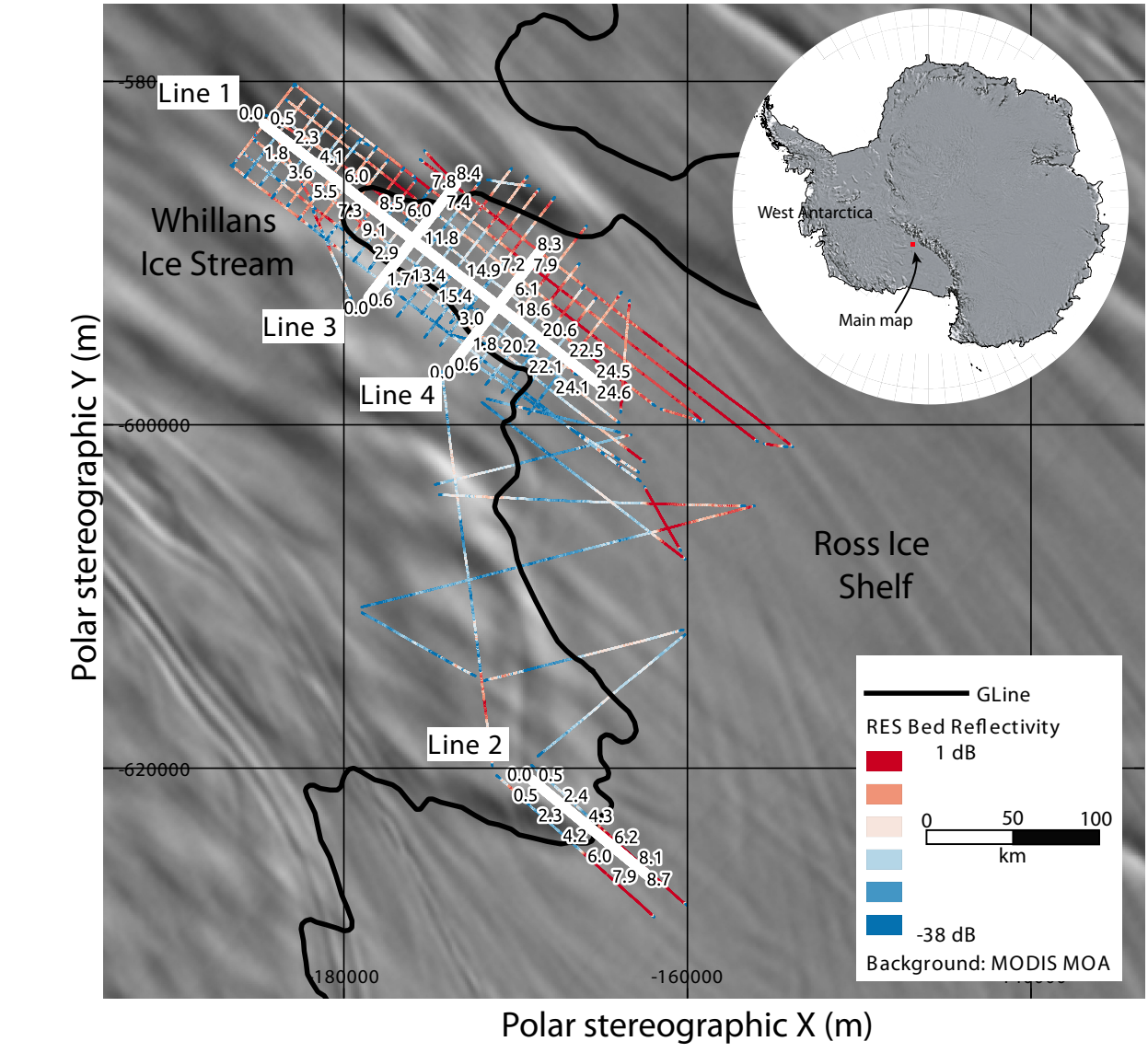

Figure 1. Location map showing the seismic profiles (white with kilometer annotations) crossing the grounding zone of Whillans Ice Stream. Radio echo sounding (RES) basal reflectivity from Christianson et al. (2016). Background imagery from MODIS MOA (Haran et al., 2005). Grounding zone from Bindschadler et al. (2011). Polar sterographic projection (meters) with a true scale at 71° south.

Acquisition used an asymmetric split spread with near and far shot-receiver offsets of 10 m and 1430 m. Seismic imaging and grounding zone determination at Whillans Ice Stream is presented in Horgan et al. (2013b).

https://doi.org/10.5194/tc-2020-147
Preprint. Discussion started: 16 July 2020

The Cryosphere Discussions
Open Access
EGU

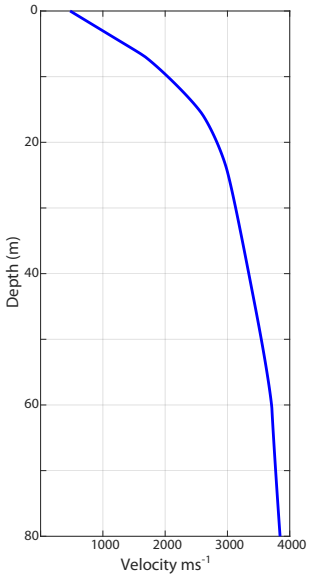

Figure 2. One dimensional compressional wave velocity profile estimated using the τ-p method.

Following Holland and Anandakrishnan (2009), the amplitudes reflected off of the base of the ice and recorded at our geophones (A_i, where i denotes the receiver index) are related to our source amplitude (A_0) by:

$$A_i = A_0 \gamma_i R(\theta) e^{-\alpha s_i}, \tag{1}$$

where $R(\theta)$ denotes the angle (θ) dependent reflection coefficient at the base of the ice described by the Zoeppritz equations (e.g. Aki and Richards, 1980). During travel along the path length (s_i) from the source to the receiver, amplitudes are modified by path effects (γ_i) and attenuation (α), all of which are discussed below.

2.1 Seismic Velocity Model

Tracing seismic ray paths between the source and receivers requires knowledge of the firn and ice column's seismic velocity. A one-dimensional (1D) velocity model was estimated using shallow seismic-refraction techniques. During shallow refraction surveying a hammer source was recorded at 0.5 m intervals with near and far offsets of 0.5 m and 579 m. A velocity model (Figure 2) was then calculated using first-break arrival times and the τ-p (intercept time–slowness) method (e.g. Shearer, 2009), which assumes that the velocity monotonically increases with depth. The bottom velocity of the model was estimated using the temperature–velocity relationship of Kohnen (1974) and an assumed ice temperature of -20°C. Implicit in our use of a 1D velocity model is an assumption that seismic velocity does not vary laterally within the survey area.

https://doi.org/10.5194/tc-2020-147
Preprint. Discussion started: 16 July 2020

2.2 Amplitude Picking

Amplitudes were picked on frequency-filtered and amplitude-scaled shot records guided by common depth point stacked profiles (Figure 3). On every shot record we attempted to digitize the direct arrival, primary bed return, and first long-path multiple of the bed return. The low impedance-contrast at the ice-bed interface meant the long-path multiple could not be reliably picked in the grounded part of the profiles. Amplitude picking selected the zero crossing preceding the side-lobe of the wavelet. Amplitude extraction was then performed on shot records with only bandpass filtering applied. Amplitudes were extracted within the wavelet encompassing the first side lobe, the central lobe, and the next side lobe. Within this wavelet, peak positive, peak negative, and root mean squared (RMS) amplitudes were extracted. We avoided picking bed returns where direct arrival energy was interfering with the bed wavelet. Our data are from ice thicknesses of approximately 730–790 m and direct arrivals interfere with the reflection from the base of the ice beyond offsets of approximately 700 m. While the channels with 5-element georods showed better signal to noise ratios for imaging, we here present an analysis of the single-string geophones as their amplitudes exhibit less channel to channel variability. Our analysis also uses the RMS amplitudes, with the positive and negative peaks used to define polarity. We tested the use of peak amplitudes and fixed wavelet length approaches and found both resulted in a greater distribution of source sizes, and less robust estimates of basal reflectivity.

2.3 Path effects

Path effects (γ_i) modify the source amplitude during its propagation to the receiver. We calculate the total path effects as

$$\gamma_i = \frac{\cos\theta_i}{s_i}\sqrt{\frac{z_0}{z_1}} \tag{2}$$

where θ_i denotes the angle between the incoming ray and normal incidence, z_0, z_1 denote the acoustic impedance at the source and receiver respectively, and s_i denotes the path length traveled between the source and receiver. Equation 2 therefore accounts for the angle at which the incoming ray arrives at the vertical-component receivers $(\cos\theta_i)$, amplitude scaling due to the different acoustic impedance at the source and receiver ($\sqrt{\frac{z_0}{z_1}}$, e.g. Shearer, 2009), and geometric spreading along the ray path $(1/s_i)$. We estimate all near-field effects using the 1D velocity model (Figure 2) and the density–compressional-wave velocity relationship of Kohnen and Bentley (1973). The high vertical gradients in density and velocity in polar firn lead to a $\cos\theta_i$ correction≈ 1, as $\theta_i \approx 0$, and a significant $\sqrt{\frac{z_0}{z_1}}$ correction $(\sim\sqrt{10})$ due to the different source and receiver burial depths.

2.4 Source size and attenuation

Source size (A_0) is often estimated using the ratio of the primary bed return amplitude (A_i) and the long path multiple amplitude $(A_{m,i})$ (e.g. Röthlisberger, 1972; Smith, 1997; Peters et al., 2008; Brisbourne et al., 2017; Zechmann et al., 2018), as this approach can remove the need for an independent estimate of attenuation. However, low impedance contrast at the bed, low signal to noise ratios, or closely spaced subglacial reflectors, can all complicate the amplitude ratio method of determining source amplitude. Here we explore this and other methods for determining the source amplitude because more-accurate source-

https://doi.org/10.5194/tc-2020-147
Preprint. Discussion started: 16 July 2020

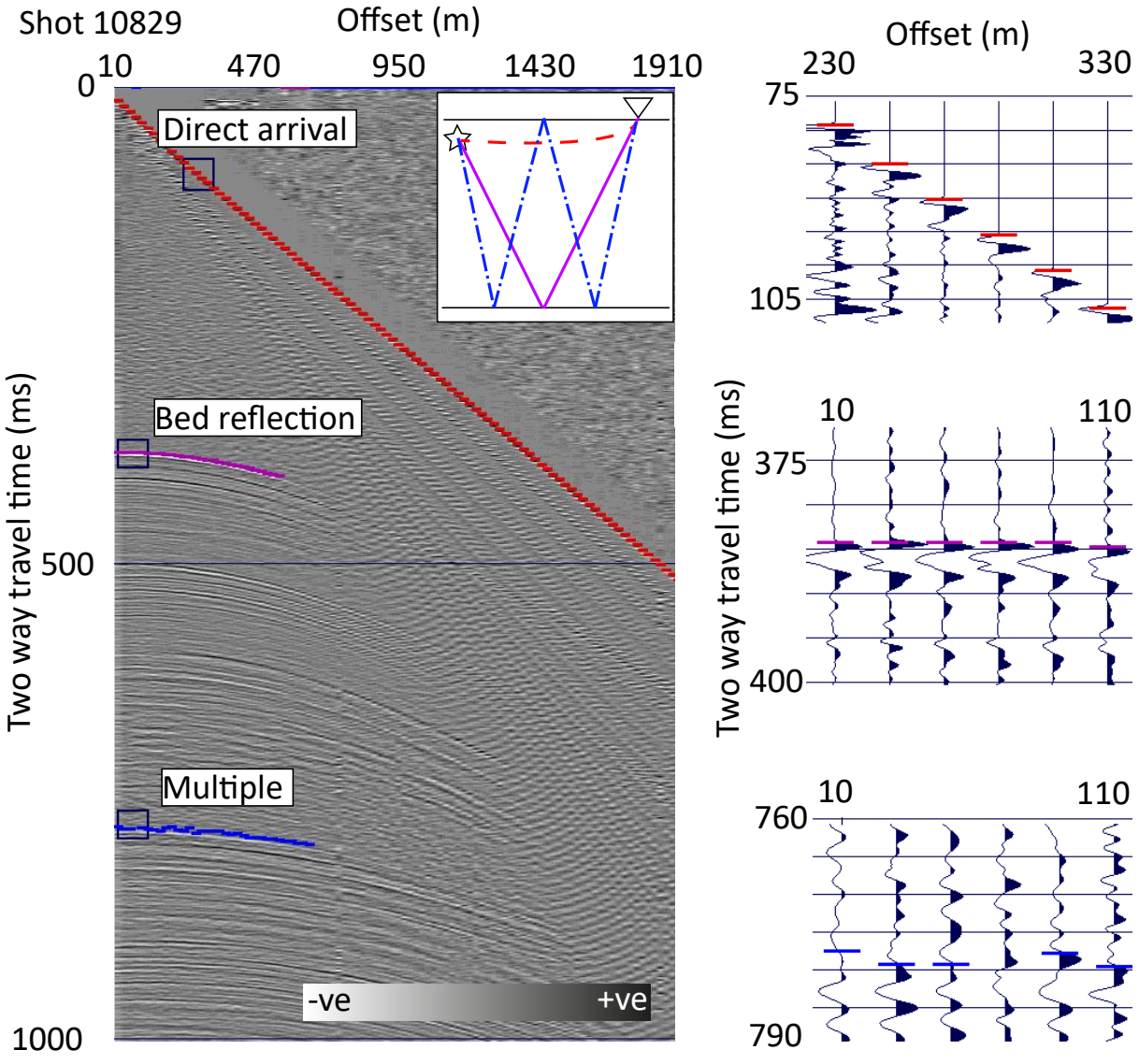

Figure 3. Left panel: example shot record from floating portion of Line 2 (Kilometer 4.8-6.7). Left panel inset shows schematic travel paths for direct (red), primary (purple), and multiple (red) rays. Right hand panels show wavelets and picks for the direct arrival (top), primary return (middle), and multiple return (bottom).

amplitude estimates will enable improved investigation of the rapid spatial transitions in basal properties resolved by the seismic surveys. These methods fall into three categories: (1) primary–multiple amplitude ratios, (2) direct arrival amplitudes, and (3) known reflector amplitudes. We present the results for each of the four profiles individually as three different source sizes and configurations were used (Figure 4, Table 1).

https://doi.org/10.5194/tc-2020-147
Preprint. Discussion started: 16 July 2020


The Cryosphere Discussions
Open Access
EGU

Here primary–multiple amplitude ratio methods for estimating A_0 follow Holland and Anandakrishnan (2009). The first method requires near-normal incidence returns but does not require knowledge of attenuation (α):

$$A_{0,i} = \frac{A_i^2}{A_{m,i}} \frac{1}{2\gamma_i}, \tag{3}$$

and the second method requires close to normal incidence returns and an estimate of attenuation:

$$A_{0,i} = \frac{A_i^2}{A_{m,i}} \frac{\gamma_{m,i}}{2\gamma_i^2} e^{\alpha(2d_i - d_{m,i})}, \tag{4}$$

where d_i and $d_{m,i}$, and γ_i and $\gamma_{m,i}$ denote the path length, and path amplitude factor (Equation 2) for the primary and multiple bed returns respectively. A_0 is then calculated as the average $A_{0,i}$ for each shot. Equations 3 and 4 give near identical A_0 estimates with root mean squared differences $\approx$0.1%. Henceforth for the amplitude ratio method we report only the results from Equation 4 with an angle cut off of $<10°$ and assuming an attenuation $\alpha = 0.27 \pm 0.13$ km^{-1} (following Horgan et al., 2011). Holland and Anandakrishnan (2009) note that Equation 4 is weakly dependent on uncertainties in α. Long-path multiples from shots in which the primary reflections were from the interface between ice and seismically thick ($>$ 5 m, see Section 4) water resulted in 60, 19, 9, and 24 estimates of A_0 for Lines 1–4, respectively (left column Figure 4, A_{0AR} columns Table 1).

Here two methods are also used to estimate source amplitude from the direct arrival amplitudes (B_i). Direct arrivals have successfully been used to determine source size (Muto et al., 2019) and to normalise shot records (Brisbourne et al., 2017). Following Holland and Anandakrishnan (2009):

$$B_i = A_0 \gamma_{d,i} e^{-\alpha s_{d,i}}, \tag{5}$$

where B_i denotes direct arrival amplitude at receiver index i, and $s_{d,i}$ and $\gamma_{d,i}$ are the direct arrival path lengths and path amplitude factors. We first estimate A_0 using the direct-path pair method of Holland and Anandakrishnan (2009) (Figure 4B,D; Table 1). This method uses receiver pairs where the ratio of path lengths $s_2/s_1 = 2$, and where the depth averaged attenuation can be assumed the same. This negates the need for an independent attenuation estimate. Our acquisition geometry did not result in pairs where $s_2/s_1 = 2$ exactly so an acceptance distance (x_1) was set such that pairs were used if $s_2 >= 2s_1 - x_1 \wedge s_2 <= 2s_1 + x_1$. We set $x_1 = 14$ m through trial and error, looking for the minimum x_1 that would result in multiple estimates of A_0 for all shots. This resulted in a mode of 8 pairs per shot (mean of 7.7, standard deviation of 3.7). A_0 direct pair estimates are shown in Figure 4 (centre left column) and Table 1 (A_{0DP} columns).

We also investigate A_0 estimation using all direct arrival amplitudes by fitting the observed B_i values to Equation 5 and minimizing the misfit to determine optimal A_0 and α values (Figure 4C,D; Table 1). We refer to this method as the direct path linear intercept method, because

$$\ln \frac{B_i}{\gamma_{d,i}} = -\alpha s_{d,i} + \ln A_0$$

shows that in $\ln \frac{Bi}{\gamma_i}$ versus $-s_i$ space every shot record should exhibit a common gradient (α), and independent y-intercepts representing $\ln A_0$. Despite this linear form we solve for best fitting parameters directly from Equation 5 using non-linear

https://doi.org/10.5194/tc-2020-147
Preprint. Discussion started: 16 July 2020

The Cryosphere Discussions

Table 1. Source size (A_0) estimates. Line 1 used a single 0.4 kg charge. Lines 2 and 4 used two 0.4 kg charges in a vertical configuration. Line 3 used one 0.4 kg charge and three 0.15 kg charges in a vertical configuration. See Section 4 for discussion.

Line	Source Size (kg)	A_{0AR} Median	A_{0AR} Mean	A_{0AR} Std	A_{0DP} Median	A_{0DP} Mean	A_{0DP} Std	A_{0LI} Median	A_{0LI} Mean	A_{0LI} Std	A_{0KR} Median	A_{0KR} Mean	A_{0KR} Std
1	0.40	1097	1076	299	229	260	131	232	288	195	420	430	61
2	0.80	1312	1424	413	171	176	93	150	188	128	606	629	164
3	0.85	691	744	288	202	220	123	197	249	169	353	367	34
4	0.80	1200	1259	242	258	290	101	239	295	167	552	544	74

Table 2. Seismic velocity and density assumed at the ice shelf base.

	V_p	V_s	ρ
Ice	3860	1930	917
Water	1440	0	1020

regression. We restrict our direct arrival analysis to returns from offsets greater than 450 m, and testing up to an offset limit of > 800 m did not result in significantly different A_0 and α estimates. A_0 direct linear intercept estimates are shown in Figure 4 (centre right column) and Table 1 (A_{0LI} columns).

Reflections from a known impedance contrast, in this case the floating ice shelf overlying the ocean cavity, allow another method of determining A_0. We estimate a best fitting A_0 for each ice shelf shot by minimizing the root-mean-squared misfit between the Zoeppritz equation reflection amplitudes for the seismic properties in Table 2, and the observed bed reflection amplitudes after correction for path effects and attenuation. This results in the same number of A_0 estimates as the amplitude ratio method. The method is insensitive to our assumption that $\alpha = 0.27 \pm 0.13$ km^{-1} as the same α used to determine A_0 is later used to determine the basal reflection coefficient. We refer to this method as the known reflector method and the resulting A_0 estimates are shown in Figure 4 (right column) and Table 1 (A_{0KR} columns).

2.5 Choosing the best A_0

The known reflector method provides our best estimate of A_0 as judged by its potential to recover accurate estimates of basal reflectivity, and its narrow normal distribution (Figure 4, Table 1). The narrow distribution indicates low source size variability, consistent with a uniform firn–ice profile, a consistent drilling depth and geophone placement, back filling all shots, and allowing at least 24 hours before detonation. We use the average amplitude for each line, which is approximately equal to the median, and adopt the standard deviation as our uncertainty.

https://doi.org/10.5194/tc-2020-147
Preprint. Discussion started: 16 July 2020

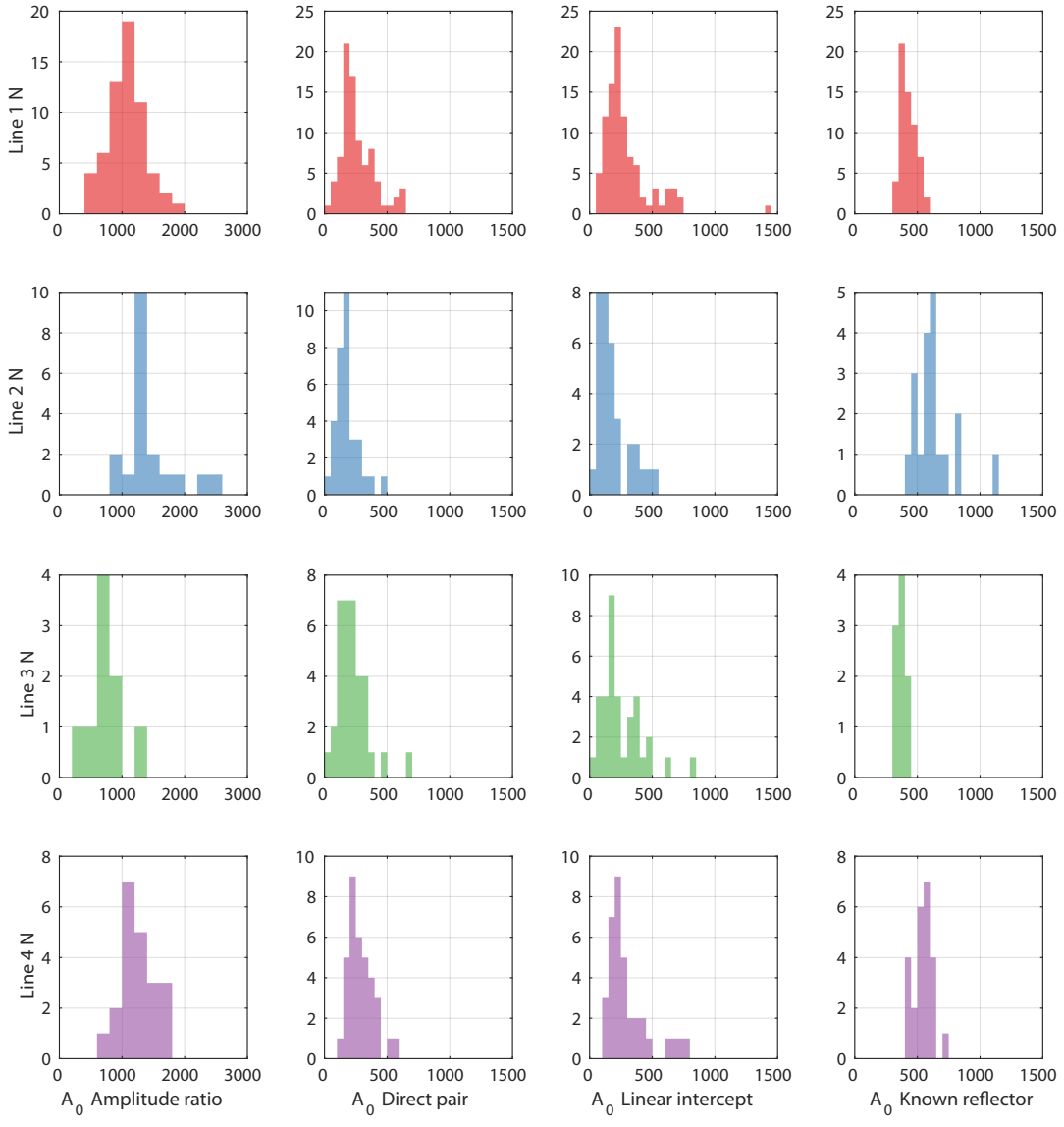

Figure 4. A_0 source size estimates for Whillans Grounding Zone Lines 1–4 (rows) using four methods (columns). Left column: A_0 estimates using the primary–multiple amplitude ratio method. Centre left column: A_0 direct pair estimates. Centre right column: A_0 linear intercept estimates. Right column: A_0 estimates from known reflection coefficient method assuming ice overlying water. (See Figure 1 for line locations.)

Both our direct path methods show large standard deviations (Table 1) and correlate poorly with our known reflector estimates (r^2 (coefficient of determination) of 0.1 for the direct pair method and 0.04 for the linear intercept method, Figure 5). The linear intercept method resulted in an average $\alpha = 1.4 \pm 0.5$ km^{-1} (mean and 1 standard deviation of the combined results for all 4 lines). Individual line average values range from 1.0–1.6 km^{-1}. These α estimates are an order of magnitude greater

https://doi.org/10.5194/tc-2020-147
Preprint. Discussion started: 16 July 2020

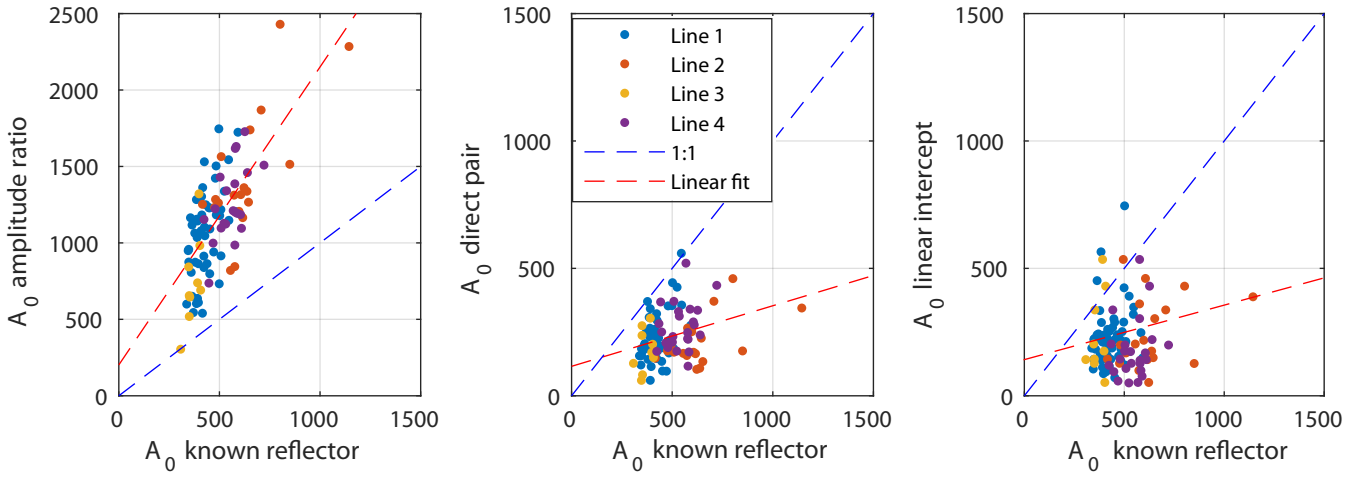

Figure 5. A_0 estimates comparisons. Left: A_0 estimates from known reflector method (abscissa) against A_0 estimates from amplitude ratio method (ordinate) (coefficient of determination (r^2) of linear regression = 0.45). Middle: A_0 estimates from known relectivity method (abscissa) against A_0 estimates from the direct pair method (ordinate) (r^2=0.10). Right: A_0 estimates from known reflector method against A_0 estimates from linear intercept method (r^2=0.04).

than commonly used published estimates and are not used in our analysis. The amplitude ratio method correlates well with the known reflector method (r^2=0.45, Figure 5). Linear regression of the known reflector estimates with the amplitude ratio estimates results in a best fitting gradient of 2.0 with an intercept of 200. However, this relationship is dependent on our estimate of α and our γ estimates, and will be discussed in Section 4.

2.6 Estimating subglacial properties

Using each line's average A_0 values from the known reflector method (Table 1, Figure 4A) we calculate the angle dependent bed reflection coefficients for each shot gather ($R(\theta)$, Equation 1). We present these in Figures 6–7 as both average values within 10 degrees of normal incidence (R_{b10}) and as intercept values (R_{bInt}) calculated from linear regression through each shot's observed $R(\theta)$ values (Figures 6A, 7A). We then calculate the optimal combination of subglacial seismic velocities (V_p, V_s) and density (ρ) (Figures 6– 7B–D) by fitting each shot's complete $R(\theta)$ to the Zoeppritz equation while imposing reasonable bounds for subglacial material following Zechmann et al. (2018), expanded to allow for an ice/water interface (Table 3). During optimisation we impose the additional constraint that the optimal V_p and V_s must result in a realistic Poisson's ratio of 0.25–0.5 (Hamilton, 1979). Optimisation minimises the root mean squared misfit between the observed amplitudes for each shot and those modelled by the Zoeppritz equations using the *fmincon* algorithm in MATLAB®. This optimisation uses a trust region approach resulting in rapid convergence. Finally we group our results using K-means clustering (Hartigan, 1975) into three groups based on each shot's R_{b10}, V_p, and ρ values (Figures 6–7B–D). We exclude V_s from this clustering analysis due to its

https://doi.org/10.5194/tc-2020-147
Preprint. Discussion started: 16 July 2020


The Cryosphere Discussions
Open Access
EGU

Table 3. Seismic velocity (V_p, V_s), density (ρ) and Poisson's Ratio (σ) bounds used for Zoeppritz fitting.

	Lower Limit	Upper Limit
V_p (m s^{-1})	1440	2300
V_s (m s^{-1})	0	1150
ρ (kg m^{-3})	1000	2500
σ	0.25	0.5

high spatial variability, the cause of which we discuss in Section 4. We estimate our uncertainties by repeating our R_b estimates and the optimisation of V_p, V_s, and ρ values using $R(\theta)$ values estimated from our A_0 uncertainty bounds.

3 Results

3.1 Reflection Coefficients and Basal Properties

Line 1 (Figure 6) exhibits generally slowly varying R_b values upstream of the grounding zone, before an abrupt change at the grounding zone (Figure 6). This change occurs over less than 500 m at approximately kilometer 9. V_p, V_s and ρ values retrieved from Zoeppritz fitting exhibit a similarly abrupt change at the grounding zone. Our clustering analysis results in the grounded portion exhibiting three substrate groups, dominated by one group (Group 1, Figure 6, Table 4). The floating portion of Line 1 is composed of one group (Group 2), with estimated V_p and ρ values consistent with water. Retrieved V_s values are variable upstream and downstream of the grounding zone, with most V_s values beneath the ice shelf equal to those expected for water. Both kilometer 3–4, and the grounding zone of Line 1 (kilometer 9) exhibit retrieved V_s and ρ values similar to those expected for water, but R_{b10} and V_p estimates suggest otherwise.

Line 2 (Figure 7, left panel) exhibits similar patterns in R_b and retrieved seismic properties to Line 1. An abrupt transition is observed at the grounding zone (kilometer 4), and the grounded and floating portions are dominated by distinct groups (Groups 1 and 2 respectively, Figure 7, Table 4). Upstream of the grounding zone two retrieved estimates exhibit properties similar to those of water (kilometer 0–0.5); however, neither are unambiguous. V_s estimates are again more variable than other parameters, with most floating shots exhibiting V_s values typical of water. Line 3 (Figure 7, middle panel) shows both rapid and gradual changes in basal properties along the profile. Rapid changes are observed either side of kilometer 7–8 where a narrow bed feature exhibits V_p and ρ estimates typical of subglacial water. Kilometer 2–4 displays a gradual change in R_b while the associated transition in V_p and ρ occurs abruptly over $<$500 m. V_s estimates are variable along the profile, and exhibit scatter within regions thought to be both grounded (kilometer 0–3) and floating (kilometer 3.5–6). Line 4 (Figure 7, right panel) is dominated by R_b, V_p and ρ estimates typical of ice over water (kilometer 1–7). The transition from these values occurs over a

https://doi.org/10.5194/tc-2020-147
Preprint. Discussion started: 16 July 2020

Table 4. Seismic properties from Zoeppritz fitting.

Line, Group	V_p (m s^{-1})	V_s (m s^{-1})	ρ (kg m^3)
Line 1, Group 1 (N=28)	1850±90	680±340	1710±120
Group 2 (N=62)	1530±100	180±300	1030±60
Group 3 (N=7)	2210±150	330±560	1160±90
Line 2, Group 1 (N=12)	1800±70	690±430	1670±90
Group 2 (N=20)	1540±90	320±380	1080±120
Group 3 (N=1)	2170	0	1000
Line 3, Group 1 (N=11)	1890±110	670±470	1720±170
Group 2 (N=16)	1520±110	340±390	1040±90
Group 3 (N=6)	1980±180	560±610	1070±90
Line 4, Group 1 (N=6)	1920±140	600±540	1640±190
Group 2 (N=25)	1480±40	290±330	1050±70
Group 3 (N=4)	1840±250	0±0	1000± 0

distance of <1 km. As with the other profiles the estimates of V_s are variable but most often the floating portion of the profile (kilometer 1–7) exhibits V_s estimates typical of water.

4 Discussion

4.1 Subglacial properties beneath Whillans Ice Stream's grounding zone

Subglacial material beneath the grounded ice stream exhibits ρ and V_p values in the range of dilatant till, but with most V_s values typical of those observed in dewatered tills (Figure 6– 7, Table 4) (Zechmann et al., 2018). Our estimates of V_p and ρ for all lines are close to those estimated by Luthra et al. (2016) in their active source seismic study of a major sticky spot beneath Whillans Ice Plain. V_s estimates from the grounding zone are greater than those estimated by Luthra et al. (2016), although they overlap within uncertainties. When compared with estimates from upstream on Whillans, where Blankenship et al. (1986) measured V_s of 150±10 m s^{-1}, our results indicate significantly stiffer till beneath the grounding zone. Compression and dewatering of subglacial till due to ice flexure within the grounding zone has been hypothesised by Walker et al. (2013), and was invoked by Christianson et al. (2013) as the cause of the enhanced internal deformation evident in radio echo sounding profiling across the grounding zone. Our finding of dewatered till is consistent with this hypothesis.

Upstream of the grounding zone several regions (e.g. Line 1 kilometer 3–4; Line 2, kilometer 0–0.5; Line 3 kilometer 7–8) exhibit properties that indicate the presence of subglacial water, although not without ambiguity. This ambiguity likely results

https://doi.org/10.5194/tc-2020-147
Preprint. Discussion started: 16 July 2020

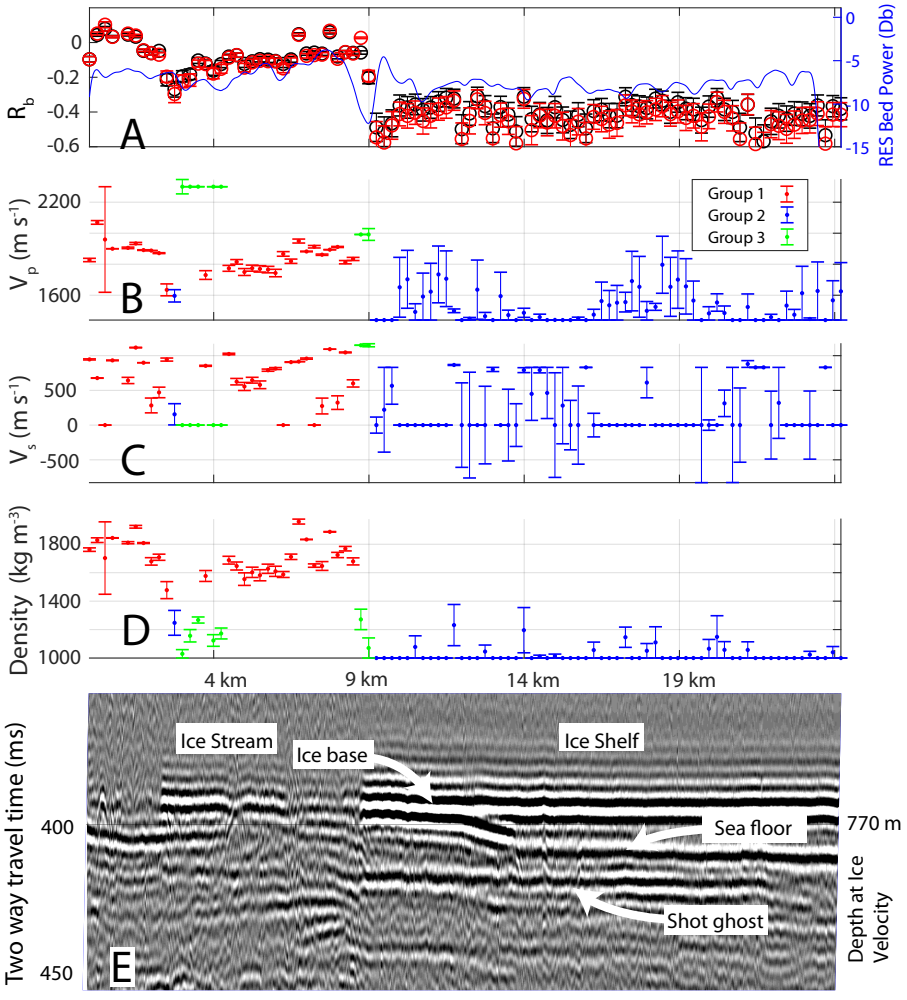

Figure 6. Line 1 (A) Seismic basal refectivity at normal incidence estimated from the average value within 10° (R_{b10}, black) and using the linear intercept method (R_{bInt}, red). Blue line shows radar basal reflectivity from Christianson et al. (2016). (B–D) V_p, V_s and ρ estimated using Zoeppritz fitting. (E) Stacked active source seismic reflection profile with ice flow from left (grounded ice stream) to right (floating ice shelf). Shot ghost denotes the short-path multiple generated by the ray path from the source to the ice-air interface then down. For location see Figure 1.

from water column thicknesses that are less than one-quarter the dominant seismic wavelength for our data, $\lambda/4 \approx 5$ m. Visual inspection of shot records shows that in these regions the thin-layer effects detailed by Booth et al. (2012) result in constructive and destructive interference of our basal wavelet, leading to best-fitting parameter combinations that are not representative of the contrast in properties. A similar phenomenon likely results in the anomalous estimated values at the grounding zone of Line 1 (Figure 6, kilometer 9) and for kilometer 7–7.5 of Line 3 (Figure 7). However, no similar attribution is possible for the V_s

https://doi.org/10.5194/tc-2020-147
Preprint. Discussion started: 16 July 2020

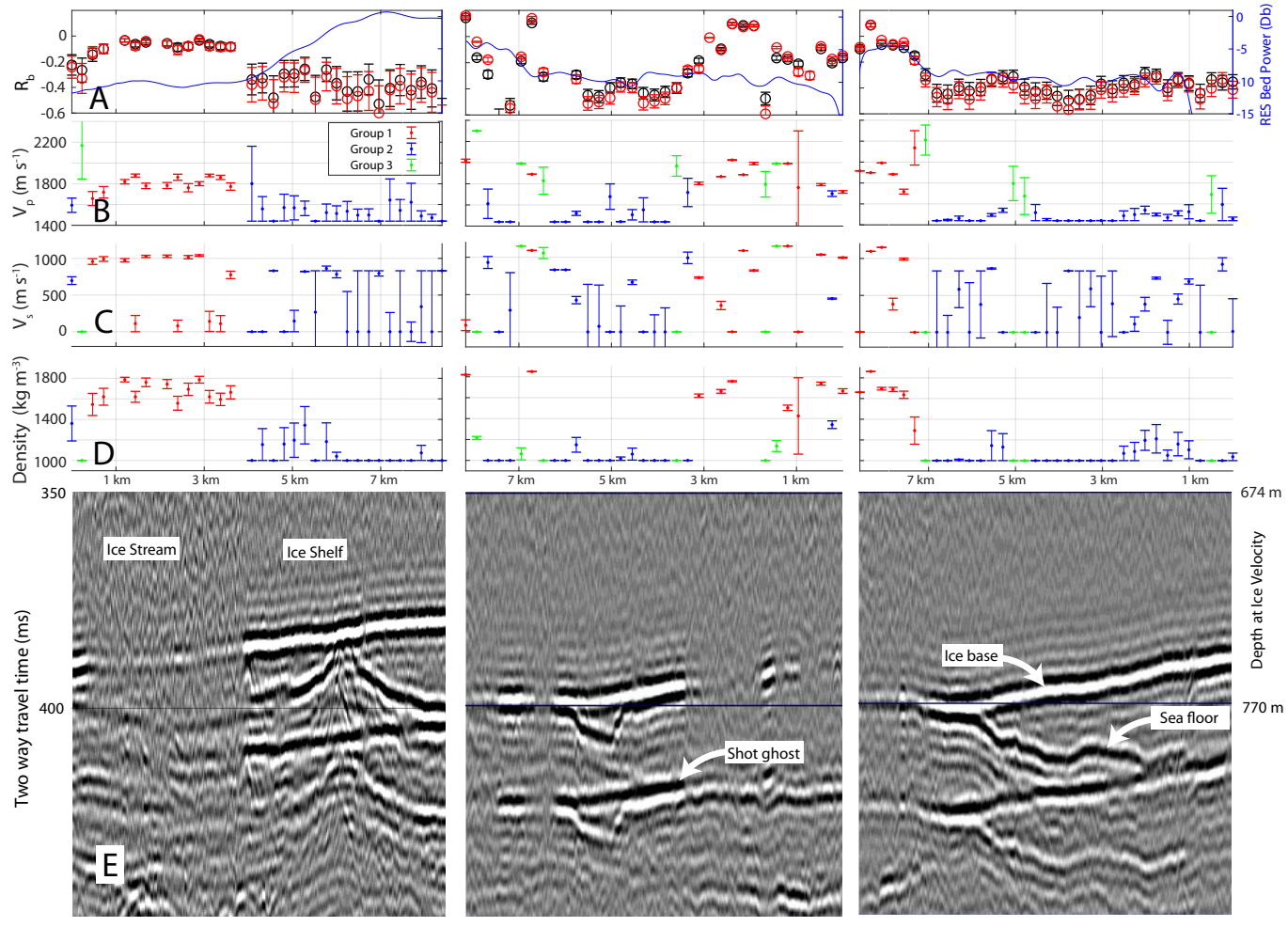

Figure 7. Lines 2 (left), 3 (middle), and 4 (right).(A) basal refectivity at normal incidence estimated from the average value within 10° (black) and using the linear intercept method (red). Blue line shows radar basal reflectivity from Christianson et al. (2016). (B–D) V_p, V_s and ρ estimated using Zoeppritz fitting. (E) Stacked active source seismic reflection profile. Line 2 is plotted flowing from grounded (left) to floating (right). Lines 3 and 4 are plotted with flow into the page. Shot ghost denotes the short-path multiple generated by the ray path from the source to the ice-air interface then down. For locations see Figure 1.

outliers in the floating portions of all lines, which instead appear to correspond to low signal to noise ratios apparent in visual inspection of the shot records.

The transition in basal properties at the grounding zone of Whillans Ice Stream is abrupt in both longitudinal lines (Lines 1–2), occurring over distances of less than 500 m. This is less than the ice thickness of 730–790 m. The transverse lines (Lines 3–4) exhibit less abrupt transitions but still show change over distances of less than 1 km. The rapid transition in basal properties indicates that the full Stokes equations are likely to be needed to be solved if the ice flow velocity field is to be accurately

https://doi.org/10.5194/tc-2020-147
Preprint. Discussion started: 16 July 2020

modelled (Pattyn et al., 2013). The radio echo sounding (RES) results of Christianson et al. (2016) provide additional insights (Figures 6A, 7A). Lines 1,3,4, which all sample the embayment in the grounding zone to the grid north (Figure 1), all exhibit a drop in RES basal reflectivity of approximately 3–5 dB as the grounding zone is crossed from the grounded ice stream to the floating ice shelf. This change occurs over similar length scales to the seismically detected transition. In contrast, Line 2, which crosses the peninsula to the grid south exhibits a gradual increase in RES basal reflectivity of approximately 10 dB after the ice goes afloat, over a distance of approximately 3 km. Christianson et al. (2016) attributes the differences in the RES-detected transitions to the presence of basal roughness (fluting) and entrained debris in the ice shelf in the embayment, and a basal interface that is becoming smoother and losing the basal debris zone due to basal melt at the peninsula. The insensitivity of seismic methods to the presence of low levels of entrained debris and fluting is evident in the abrupt transition in basal properties observed at the Line 2 transition (Figure 6). Our seismic records lack evidence of englacial reflectivity near the bed that could be attributed to sufficiently abundant englacial debris (Bentley, 1971). The contrast between the RES and active source seismic views of the grounding zone highlights the different and complementary sensitivities of the two methods.

4.2 Estimating A_0

Our preferred method of estimating source size is only possible when a portion of the survey area contains a known reflection interface. Comparison with other methods used to estimate A_0 demonstrates the efficacy of the commonly employed amplitude ratio method (Figure 5). A_0 estimated using the amplitude ratio method was, however, approximately twice that estimated using our known reflector method (Figure 5). The discrepancy between the methods indicates that attenuation (α) and path amplitude factors (γ) remain areas of uncertainty, overcome here by our use of a known reflector. In the absence of reliable A_0 estimates, other attributes of the amplitude reflection curve such as the angle of phase change (e.g. Anandakrishnan et al., 2003) can be effective predictors of subglacial geology. Direct path methods for A_0 estimation have been successfully employed elsewhere (Muto et al., 2019), and greatly simplify $R(\theta)$ recovery. Muto et al. (2019) presented data where the sources were buried at 40–50 m depth, compared to our 27 m, and their signal to noise ratios are high as evident in their imaging of englacial seismic reflectivity. The poor correlation between our known-reflector and direct-path A_0 estimates (Figure 4) shows that further investigation of direct path methods is warranted. Both the direct path methods we present would benefit from a greater offset distribution, and the direct pair method would benefit from a greater number of path combinations where $s_2/s_1 = 2$ than was available to us. Also, the path effects (γ_i) experienced by the direct ray are likely to be inadequately captured by our approach due to the possibility of unaccounted for energy loss and more complex travel paths than those predicted within the firn.

Our Zoeppritz fitting methodology is skilled at recovering both V_p and ρ as demonstrated in the floating portions of all lines where the recovered values are those expected for water (see Table 4 Group 2 estimates). The methodology is less skillful at recovering V_s, likely due to the weaker dependence of the shape of the $R(\theta)$ curve on V_s for the angles we observe. We recover the near zero V_s typical of water for 73 of the 112 floating shots in our survey. Estimating V_s, along with ρ allows the shear modulus to be estimated, which can be used to calculate the effective pressure in the till (Luthra et al., 2016). This provides a more direct link between seismic observations and till properties than is otherwise possible from estimates of reflectivity (R_b)

https://doi.org/10.5194/tc-2020-147
Preprint. Discussion started: 16 July 2020

alone. An acquisition geometry that covered greater angles would improve our ability to estimate V_s; however, limitations due to interference from direct arrivals would still exist. These limitations could be overcome by observing much greater offsets, where direct arrivals no longer interfere with the bed return, or surveying in regions of greater ice thickness.

Using multiple charge sizes and configurations also highlights the importance of source configuration. Line 3, which consisted of the largest charges by weight (0.85 kg) resulted in the lowest A_0 estimates calculated from both the known reflector method and the amplitude ratio method. The charges for Line 3 were made up of a stack of a single 0.4 kg charge, and three narrower 0.15 kg charges. These narrower charges were likely less well coupled with the shot hole wall, and the longer linear configuration resulted in a less effective source. A shorter interval between shot loading and detonation may have also been a factor here as Line 3 was shot within 1–2 days of loading.

5 Conclusions

Subglacial material beneath Whillans Ice Stream's grounding zone is relatively stiff and is seismically more similar to a subglacial sticky spot than to deforming till. Thin water bodies are detected upstream of the grounding zone. While our methods are not able to determine the process of stiffening at the grounding zone and ponding upstream, our observations are consistent with Walker et al. (2013), who model the tidal deflection of a viscoelastic beam (the ice stream–ice shelf) pivoting around a fulcrum at the grounding line. This model predicts both the strengthening of subglacial material at the grounding zone, and subglacial pressure gradients that would promote the flow of water upstream of the grounding zone. The seismically determined transition in bed properties is abrupt, occurring over distances of 500-1000 m. This differs from the transition imaged using RES, which detects both an abrupt transition and a gradual one at the embayment and promontory respectively Christianson et al. (2013).

Our comparison of methods used to determine source size (A_0) shows that the commonly employed amplitude-ratio method correlates well with the known reflector method available to us. However, our comparison also highlights that path effects (γ_i) are incompletely modelled by the methods employed here and elsewhere. Our findings also reinforce the need for consistency in source placement, configuration, and time between burial and detonation. Overall our methods are skilled at retrieving basal properties at relatively high spatial resolution where the thickness of the subglacial material is sufficient to prevent thin film effects ($> \lambda/4$). Both V_p and ρ are reliably retrieved, while V_s is recovered but less consistently. While we are currently unable to accurately recover seismic properties for what appear to be thin water layers, our methods also show promise here. These thin layers are pertinent for ice flow, and techniques such as full waveform inversion are likely to prove useful here. These methods, which invert not just for a single amplitude of the basal return but the full time series, have been successful applied to other environments where thin layers with large contrasts in seismic properties have been investigated (e.g. Pecher et al., 1996).

https://doi.org/10.5194/tc-2020-147
Preprint. Discussion started: 16 July 2020

Code and data availability. Data analysis and modelling used MATLAB® and the CREWES Matlab Toolbox (www.crewes.org). Seismic data processing and picking was performed using GLOBE Claritas (www.globeclaritas.com). Amplitude data are available at PANGEA (www.pangaea.de/ DOI pending.)

Competing interests. No competing interests are present.

Acknowledgements. We are grateful to Lucas Beem, Rory Hart, Matthew Hill, Benjamin Petersen, and Matthew Seigfried for assistance in the field. HJH thanks Roger Clark for helpful correspondence early in this study. This study was funded by US National Science Foundation grants to the CReSIS (0852697), and WISSARD (0838764, 0838763) projects. HJH acknowledges funding from a Rutherford Discovery Fellowship and Project-1 of the New Zealand Antarctic Science Platform.

https://doi.org/10.5194/tc-2020-147
Preprint. Discussion started: 16 July 2020

References

Aki, K. and Richards, P. G.: Quantitive Seismology. Theory and Methods, W.H. Freeman and Co., 1980.

Alley, R. B.: In Search of Ice-Stream Sticky Spots, J. Glaciol., 39, 447–454, 1993.

Alley, R. B., Blankenship, D. D., Bentley, C. R., and Rooney, S. T.: Deformation of Till Beneath Ice Stream B, West Antarctica., Nature, 322, 57–59, 1986.

Alley, R. B., Blankenship, D. D., Bentley, C. R., and Rooney, S. T.: Till beneath Ice Stream B, 3, Till Deformation: Evidence and Implications, J. Geophys. Res., 92, 8921–8929, 1987.

Alley, R. B., Blankenship, D. D., Rooney, S. T., and Bentley, C. R.: Sedimentation beneath ice shelves - the view from Ice Stream B, Marine Geology, 85, 101–120, 1989.

Alley, R. B., Anandakrishnan, S., Dupont, T., Parizek, B. R., and Pollard, D.: Effect of Sedimentation on Ice-Sheet Grounding-Line Stability, Science, 315, 1838–1841, 2007.

Anandakrishnan, S.: Dilatant till layer near the onset of streaming flow of Ice Stream C, determined by AVO (Amplitude vs. Offset) analysis, Ann. Glaciol., 36, 283–287, 2003.

Anandakrishnan, S. and Alley, R. B.: Ice Stream C, Antarctica, Sticky-Spots Detected by Microearthquake Monitoring, Ann. Glaciol., 20, 183–186, 1994.

Anandakrishnan, S., Blankenship, D. D., Alley, R. B., and Stoffa., P. L.: Influence of subglacial geology on the position of a West Antarctica ice stream from seismic measurements, Nature, 394, 62–65, 1998.

Anandakrishnan, S., Voigt, D. E., Alley, R. B., and King, M. A.: Ice stream D flow speed is strongly modulated by the tide beneath the Ross Ice Shelf, Geophysical Research Letters, 30, 13–1–13–7, 2003.

Anandakrishnan, S., Catania, G. A., Alley, R. B., and Horgan, H. J.: Discovery of Till Deposition at the Grounding Line of Whillans Ice Stream, Science, 315, 1835–1838, 2007.

Barcilon, V. and MacAyeal, D.: Steady flow of a viscous ice stream across a no-slip/free-slip transition at the bed, Journal of Glaciology, 39, 167–185, 1993.

Bentley, C. R.: Seismic evidence for moraine within the basal Antarctic ice sheet, in: Antarctic snow and ice studies, II, Antarctic Research Series, edited by Crary, A., vol. 16, American Geophysical Union, 1971.

Bindschadler, R., Choi, H., Wichlacz, A., Bingham, R., Bohlander, J., Brunt, K., Corr, H., Drews, R., Fricker, H., Hall, M., Hindmarsh, R., Kohler, J., Padman, L., Rack, W., Rotschky, G., Urbini, S., Vornberger, P., and Young, N.: Getting around Antarctica: new high-resolution mappings of the grounded and freely-floating boundaries of the Antarctic ice sheet created for the International Polar Year, The Cryosphere, 5, 569–588, 2011.

Blankenship, D. D., Bentley, C. R., Rooney, S. T., and Alley, R. B.: Seismic Measurements Reveal a Saturated, Porous Layer Beneath an Active Antarctic Ice Stream, Nature, 322, 54–57, 1986.

Blankenship, D. D., Bentley, C. R., Rooney, S. T., and Alley, R. B.: Till Beneath Ice Stream B, 1, Properties Derived from Seismic Travel Times, J. Geophys. Res., 92, 8903–8911, 1987.

Booth, A. D., Clark, R. A., Kulessa, B., Murray, T., Carter, J., Doyle, S. H., and Hubbard, A. L.: Thin-layer effects in glaciological seismic amplitude-versus-angle (AVA) analysis: implications for characterising a subglacial till unit, Russell Glacier, West Greenland, Cryosphere, 6, 909–922, 2012.

https://doi.org/10.5194/tc-2020-147
Preprint. Discussion started: 16 July 2020

Brisbourne, A. M., Smith, A. M., Vaughan, D. G., King, E. C., Davies, D., Bingham, R. G., Smith, E. C., Nias, I. J., and Rosier, S. H. R.: Bed conditions of Pine Island Glacier, West Antarctica, Journal of Geophysical Research: Earth Surface, 122, 419–433, 2017.

Christianson, K., Parizek, B. R., Alley, R. B., Horgan, H. J., Jacobel, R. W., Anandakrishnan, S., Keisling, B. A., Craig, B. D., and Muto, A.: Ice sheet grounding zone stabilization due to till compaction, Geophysical Research Letters, 40, 5406–5411, 2013.

Christianson, K., Jacobel, R. W., Horgan, H. J., Alley, R. B., Anandakrishnan, S., Holland, D. M., and DallaSanta, K. J.: Basal conditions at the grounding zone of Whillans Ice Stream, West Antarctica, from ice-penetrating radar, Journal of Geophysical Research: Earth Surface, 121, 1954–1983, 2016.

Hamilton, E. L.: V_p/V_s and Poisson's ratios in marine sediments and rocks, The Journal of the Acoustical Society of America, 66, 1093–1101, 1979.

Haran, T., Bohlander, J., Scambos, T., and Fahnestock, M.: MODIS mosaic of Antarctica (MOA) image map, NSIDC Digital media, 2005.

Hartigan, J. A.: Clustering algorithms, Wiley, 1975.

Holland, C. and Anandakrishnan, S.: Subglacial seismic reflection strategies when source amplitude and medium attenuation are poorly known, Journal of Glaciology, 55, 931–937, 2009.

Horgan, H. J., Anandakrishnan, S., Alley, R. B., Burkett, P. G., and Peters, L. E.: Englacial seismic reflectivity – Imaging crystal orientation fabric in West Antarctica, Journal of Glaciology, 57, 639–650, 2011.

Horgan, H. J., Alley, R. B., Christianson, K., Jacobel, R. W., Anandakrishnan, S., Muto, A., Beem, L. H., and Siegfried, M. R.: Estuaries beneath ice sheets, Geology, 2013a.

Horgan, H. J., Christianson, K., Jacobel, R. W., Anandakrishnan, S., and Alley, R. B.: Sediment deposition at the modern grounding zone of Whillans Ice Stream, West Antarctica, Geophysical Research Letters, 40, 3934–3939, 2013b.

Kamb, B.: Basal zone of the West Antarctic ice streams and its role in the lubrication of their rapid motion, in: The West Antarctic Ice Sheet: Behavior and Environment, edited by Alley, R. B. and Bindschadler, R. A., vol. 77 of *Antarctic Research Series*, pp. 157–200, AGU, 2001.

Kohnen, H.: The temperature dependence of seismic waves in ice, Journal of Glaciology, 13, 144–147, 1974.

Kohnen, H. and Bentley, C. R.: Seismic Refraction and Reflection measurements at "Byrd" Station, Antarctica, Journal of Glaciology, 12, 101–111, 1973.

Luthra, T., Anandakrishnan, S., Winberry, J. P., Alley, R. B., and Holschuh, N.: Basal characteristics of the main sticky spot on the ice plain of Whillans Ice Stream, Antarctica, Earth and Planetary Science Letters, 440, 12 – 19, https://doi.org/https://doi.org/10.1016/j.epsl.2016.01.035, http://www.sciencedirect.com/science/article/pii/S0012821X16300103, 2016.

Luthra, T., Peters, L. E., Anandakrishnan, S., Alley, R. B., Holschuh, N., and Smith, A. M.: Characteristics of the sticky spot of Kamb Ice Stream, West Antarctica, Journal of Geophysical Research: Earth Surface, 122, 641–653, 2017.

MacAyeal, D. R., Bindschadler, R. A., and Scambos, T. A.: Basal Friction of Ice Stream E, West Antarctica, Journal of Glaciology, 41, 247–262, 1995.

Muto, A., Anandakrishnan, S., Alley, R. B., Horgan, H. J., Parizek, B. R., Koellner, S., Christianson, K., and Holschuh, N.: Relating bed character and subglacial morphology using seismic data from Thwaites Glacier, West Antarctica, Earth and Planetary Science Letters, 507, 199–206, 2019.

Nowicki, S. M. J. and Wingham, D. J.: Conditions for a steady ice sheet–ice shelf junction, Earth and Planetary Science Letters, 265, 246–255, 2008.

https://doi.org/10.5194/tc-2020-147
Preprint. Discussion started: 16 July 2020

Pattyn, F., Perichon, L., Durand, G., Favier, L., Gagliardini, O., Hindmarsh, R. C. A., Zwinger, T., Albrecht, T., Cornford, S., Docquier, D., and et al.: Grounding-line migration in plan-view marine ice-sheet models: results of the ice2sea MISMIP3d intercomparison, Journal of Glaciology, 59, 410–422, 2013.

Pecher, I. A., Minshull, T. A., Singh, S. C., and von Huene, R.: Velocity structure of a bottom simulating reflector offshore Peru: Results from full waveform inversion, Earth and Planetary Science Letters, 139, 459 – 469, https://doi.org/https://doi.org/10.1016/0012-821X(95)00242-5, http://www.sciencedirect.com/science/article/pii/0012821X95002425, 1996.

Peters, L. E., Anandakrishnan, S., Holland, C. W., Horgan, H. J., Blankenship, D. D., and Voigt, D. E.: Seismic detection of a subglacial lake near the South Pole, Antarctica, Geophysical Research Letters, 35, 1–5, 2008.

Pratt, M. J., Winberry, J. P., Wiens, D. A., Anandakrishnan, S., and Alley, R. B.: Seismic and geodetic evidence for grounding-line control of Whillans Ice Stream stick-slip events, Journal of Geophysical Research: Earth Surface, 119, 333–348, 2014.

Röthlisberger, H.: Seismic exploration in cold regions, Tech. rep., Cold regions research and engineering lab, Hanover NH, 1972.

Schoof, C.: Ice sheet grounding line dynamics: steady states, stability and hysteresis, Journal of Geophysical Research, 112, 2007.

Shearer, P. M.: Introduction to seismology, Cambridge University Press, 2009.

Siegert, M. J., Welch, B. C., Morse, D. L., Vieli, A., Blankenship, D. D., Joughin, I., King, E. C., Leysinger Vieli, G., Payne, A. J., and Jacobel, R. W.: Ice flow direction changes in interior West Antarctica, Science, 305, 1948–1951, 2004.

Smith, A. M.: Basal conditions on Rutford Ice Stream, West Antarctica, from seismic observations, Journal of Geophysical Research, 102, 543–552, 1997.

Smith, A. M.: Subglacial bed properties from normal-incidence seismic reflection data, Journal of environmental and engineering geophysics, 12, 3–13, 2007.

Voigt, D. E., Peters, L. E., and Anandakrishnan, S.: 'Georods': the development of a four-element geophone for improved seismic imaging of glaciers and ice sheets, Annals of Glaciology, 54, 142–148, https://doi.org/10.3189/2013AoG64A432, 2013.

Walker, R. T., Parizek, B. R., Alley, R. B., Anandakrishnan, S., Riverman, K. L., and Christinason, K.: Ice-shelf tidal flexure and subglacial pressure variations, Earth and Planetary Science Letters, 361, 422–428, 2013.

Winberry, J. P., Anandakrishnan, S., Wiens, D. A., Alley, R. B., and Christianson, K.: Dynamics of stick-slip motion, Whillans Ice Stream, Antarctica, Earth and Planetary Science Letters, 305, 283–289, 2011.

Zechmann, J. M., Booth, A. D., Truffer, M., Gusmeroli, A., Amundson, J. M., and Larsen, C. F.: Active seismic studies in valley glacier settings: strategies and limitations, Journal of Glaciology, 64, 796–810, 2018.